Through thickness variations of deformation texture in round profile extrusions of 6063-type aluminium alloy: experiments, FEM and crystal plasticity modelling

Kai Zhang[a,b*], Knut Marthinsen[a], Bjørn Holmedal[a], Trond Aukrust[c], Antonio Segatori[b]

[a]*Department of Materials Science and Engineering, Norwegian University of Science and Technology, NO-7491 Trondheim, Norway*
[b]*Innovation & Technology – Europe, Extruded Solutions, Hydro, SE-61281 Finspång, Sweden.*
[c]*SINTEF Materials and Chemistry,PO Box 124 Blindern, 0314 Oslo, Norway*

Abstract

The deformation texture and its through-thickness heterogeneity for an extruded round profile are experimentally measured by the electron back-scatter diffraction technique (EBSD), and numerically modelled by coupling FEM flow simulation and crystal plasticity simulations. Deformation histories are extracted from the FEM flow simulation. The billet material was a type of 6063 aluminium alloy. Small-scale round profiles were extruded at 300 °C in a lab extrusion setup featuring immediate water quenching at the end of deformation, keeping the profile essentially in the deformed state. The deformation texture is a strong <111> and weak <100> duplex fibre texture in the centre region, whereas the texture is weaker and rotated when approaching the surface. The full-constraint Taylor and the Advanced-lamel model (Alamel) were employed and evaluated for texture predictions. Both models give similar predictions as the experiments. The Alamel model performs better in terms of both global and through-thickness texture predictions. Analysing the deformation history from the FEM simulations reveals that the deformation condition is close to ideal uniaxial tensile deformation in the centre, whereas it is an approximate plane-strain deformation with superimposed simple shear deformation near the surface region. It is concluded that the texture through-thickness gradient can be successfully predicted by coupling FEM and Alamel model for the studied profile. The texture heterogeneity is mainly attributed to the deformation heterogeneity across the thickness.

* Corresponding author.
Innovation & Technology – Europe, Extruded Solutions, Hydro, 61381, Finspång, Sweden.
E-mail address: Kai.Zhang@hydro.com; kaiz.academic@gmail.com

Keywords: Aluminium alloy, extrusion, texture, EBSD, FEM, crystal plasticity

1. Introduction

Aluminium extrusion profiles are integral to the construction, electronics and manufacturing industries nowadays. The performance of extrusion profiles is strongly dependent on its microstructure and texture. Hence, it is of both academic and industrial interests to able to understand and model the microstructure and texture evolution during extrusion.

The deformation texture and its through thickness gradient have been reported for cylindrical and flat extrusion profiles in the literature [1-3]. By indirect extrusion of an AA 6082 alloy with dispersoids that prevented recrystallization [1], the round profiles had a combined <100> and <111> duplex fibre texture, where the <111> fibre was sharper, except at the largest extrusion temperature of 540 °C. Towards the surface, the two fibres were significantly rotated. The duplex fibre texture showed extrusion temperature dependence. For the case of direct extrusion, such duplex fibre texture has also been reported [4, 5]. The deformation texture for the extruded flat profile studied in reference [3] consisted of a strong β-beta fibre in the centre sections, while towards the surface the β-beta fibre was rotated. The thickness variation of the texture showed alloy dependence.

By coupling FEM flow simulation and crystal plasticity models, deformation texture after extrusion can been predicted. Aukrust et al. [2] employed FC- and RC- Taylor model to predict the deformation texture for flat profile extrusions, while Perocheau and Driver [6] employed the Relaxed-Constraints (RC) Taylor hypothesis and a viscoplastic constitutive law. Compared to experiments, the deformation texture and its through-thickness gradient were captured in a qualitative manner, but the predictions were improved by considering the non-octahedral slip systems for high-temperature deformations [2, 6]. More recently, the overall deformation texture for extruded round profiles has been modelled by the FC-Taylor models and Alamel-type models using deformation histories along particle paths from FEM simulations by the current authors [7]. The Alamel model gave the best predictions compared to the experiments. However, the through thickness gradients of the texture was not considered in that work. As a continuation of the previous work [7], the through-thickness gradient of the

deformation texture for round profiles has been investigated both experimentally and numerically in this work.

Due to the presence of frictions between the billet material and the tools, the deformation across the thickness of extruded profiles is not uniform. The shear deformation is larger at the surface than the centre of the profile. However, a quantitative description of the heterogeneity of deformation, especially the shear deformation, has so far not been extensively reported in the literature. In the current work, we have analysed and calculated the deformation tensors along the thickness based on the deformation histories extracted from FEM simulations, using knowledge from continuum mechanics. The observed texture gradients are also correlated with the deformation heterogeneity.

2. Material and experiments

The billet material was a type of 6063 aluminium alloy with chemical composition in wt%: Si 0.4; Mg 0.5; Fe 0.096; Mn 0.017; Ti 0.01 and Al remaining[†]. It was produced by DC casting and homogenized according to standard industrial practice. The initial texture of the billet is random and the average grain size is about 90 µm. The billet was of 20.5 mm diameter and 22 mm length, while the profile was a 3mm diameter rod. Hence, the extrusion ratio was 46.7 and the average accumulated strain was 3.9. The die had a recessed pocket of 8 mm diameter and 1 mm depth, and the parallel bearing was 3 mm long. Two K-type 0.5mm diameter thermocouples were inserted in the die on the aluminium-steel interface. One thermocouple was placed on the die face, the second in the middle of the bearing in direct contact with the aluminium to record the temperature during the entire extrusion cycle.

The extrusion was performed at 300°C with a ram speed of 4.5 mm/s and a ram stroke of 9 mm. This accounts for an extrusion time of 2 seconds, followed by immediate water quenching of the profile together with the remaining billet material left in the container (i.e. the butt end) and the die. The extrusion temperature was chosen in the purpose of suppressing the static recrystallization. The chosen ram speed was chosen to give similar profile exit speed as in the industrial practice of similar alloys. The ram

[†] It is the same material as described in the reference [7]. The aluminium alloy 6463 is a type of 6063 aluminium alloy.

stroke was limited by the length of container which is very short in the employed mini-press set-up. The material was cooled below 300°C within 1.2 seconds after the end of deformation, reading from the recorded temperature history by the installed thermocouple in the bearing. The fast cooling makes it possible to preserve the deformation microstructure.

The microstructure was measured by the electron back-scatter diffraction (EBSD) technique in a field emission scanning electron microscope (FESEM). The scan was made on the diameter direction (DD) and extrusion direction (ED) plane, covering from the central axis of the profile to the surface. Two similar such through thickness scans were carried out to get reliable results. The scanned areas were positioned very close to the exit of the bearing for two reasons. Firstly the air exposure time after extrusion and before quenching is small for this region. Hence, there is limited time for static recovery and recrystallization. Secondly, steady-state deformation conditions should be a reasonable assumption for this region which is far from the front tip. In the EBSD experiments, the step size was 2 μm for measuring texture, while a smaller step size 0.4 μm was used to reveal the subgrain structure for selected areas. The results were analysed using the TSL OIM software. The orientation distribution function (ODF) was calculated using all scanning points by the series expansion method with $l_{\max} = 22$ and a Gaussian half-width of 5°, while the textures are mainly represented by calculated pole figures (PF) in the following. Triclinic sample symmetry was assumed.

The EBSD scans are divided into four concentric annuli, according to their distance from the axis in terms of percentage of the outer radius of the profile. The through-thickness variation of the texture is evaluated in these four annular sections. The definitions of the four sections are listed in Table 1.

Table 1 Four through thickness annular sections defined by the relative distance to the axis and corresponding selected particle paths in the FEM flow model

Sections	Radius range	Particle paths
I	0-40 %	s = 0.05; 0.20; 0.40
II	40-70 %	s = 0.40; 0.55; 0.70
III	70-90 %	s = 0.70; 0.80; 0.90
IV	90%-100 %	s = 0.90; 0.95; 0.99

3. FEM simulation and crystal plasticity modelling

3.1. FEM modelling

The material flow during extrusion was simulated using a commercial FEM code HyperXtrude assuming steady-state flow. Due to the symmetry of the extrusion profile and the set-up, only a small sector with symmetry planes on each side was simulated. Hexahedral brick elements were used. Very fine mesh resolution was applied in the bearing channel region to give the deformation fields there with good accuracy, see Fig. 1 (a). The container and the die were represented by rigid boundaries towards the aluminium. The temperature of the container and die was set to be 300 °C. Full sticking and a heat transfer coefficient of 10000 W/(m^{2}K) were assumed between the aluminium and the container and between the aluminium and the die face. However, in the bearing channel, where parallel bearings were used in the experiments, full slip condition were used in the simulations, as it is expected that the bearings were relieved due to die deflection during extrusion.

The constitutive equation applied to describe the hot deformation during the extrusion, is the Sellars-Tegart model [8, 9]. The steady state effective flow stress is defined as

$$\bar{\sigma}' = \frac{1}{\alpha}\sinh^{-1}\left(\frac{Z}{A}\right)^{1/n} \quad (1)$$

where $Z = \dot{\bar{\varepsilon}} e^{Q/RT}$ is the Zener-Hollomon parameter, Q is the activation energy, R is the universal gas constant, T is the absolute temperature and α, A, n and Q are temperature independent material constants. The values used for the current material are cited from the literature [10, 11] and compiled in Table 2.

Table 2 Material constants in constitutive equation used for AA6063.

α (MPa^{-1})	ln A (s^{-1})	n	Q (J mol^{-1})
0.04	22.5	5.385	141 500

The deformation histories were recorded along 9 particle paths and exported for further analysis and texture post-simulations. All the particle paths were selected on the central symmetry plane of the model, and all paths end at the exit of the 3 mm long bearing channel at their respective radii in the extruded rod, as shown in Fig. 1 (b) and listed in Table 1.

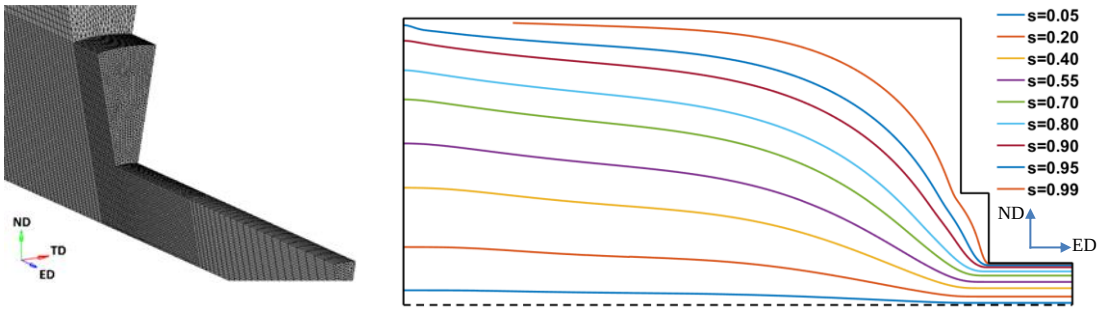

(a) (b)

Fig. 1 FEM flow simulation: (a) a region of 3D FEM model with mesh near the exit and bearing, and (b) trajectories of the 9 particle paths for recording deformation histories.

3.2. Crystal plasticity modelling

The deformation texture predictions were performed using two different crystal plasticity models, i.e. the FC-Taylor and the advanced Lamel model (Alamel).

The FC-Taylor model assumes that each single crystal experiences the same deformation as the polycrystalline aggregate [12]. Hence, grain interactions are ignored in the FC-Taylor model. Local interactions across grain boundaries are considered in Alamel-type models by relaxing the constraints on the shear strain components while imposing constraints on the corresponding stress component. The Alamel model considers a cluster containing a common grain boundary and the two adjunct grains or regions. The shear components related with the normal of the common grain boundary can be relaxed in the Alamel model [13], while the in-plane shear can be further relaxed in the Alamel T3 model [14]. The grain boundary is represented by its normal vector in the Alamel-type models.

Only the octahedral slip sytems {111}<110> are considered here. Non-octahedral slip systems [6] are excluded due to that the extrusion temperature is relatively low. The starting random texture of the billet is represented by a set of 8000 randomly distributed orientations. The assumed grain interactions take place on the common grain boundary shared by two adjacent grains in Alamel-type models. The initial orientations of the grain boundaries are defined as a set of 2000 randomly distributed normal vectors in the spatial space, and they will re-orientate during the deformation.

The crystal plasticity models apply the deformation histories exported from the FEM continuum plasticity flow simulations, particularly the velocity gradient tensor $\mathbf{L}$ and the time increment Δt, to update the texture. The final deformation texture is output and analysed also using the TSL-OIM software.

To quantitatively evaluate the simulated deformation texture, the normalized difference texture index, ID_N for comparing two textures, is adopted here as

$$ID_N = \frac{\int \left(f^{\mathrm{S}}(g) - f^{\exp}(g) \right)^2 dg}{\int \left(f^{\exp}(g) \right)^2 dg} \tag{2}$$

where $f^{\mathrm{S}}(g)$ and $f^{\exp}(g)$ are the ODFs of the predicted texture and the experimental measurements, respectively [13]. The integral is taken over the entire orientation space. Both major and minor texture components are taken into account when calculating the ID_N.

3.3. Deformation analysis methodology

The exported deformation histories from FEM flow simulations include extensive information, e.g. the temperature T, the stress tensor $\boldsymbol{\sigma}$, the velocity $\mathbf{v}$, velocity gradient tensor $\mathbf{L}$ etc. Both $\mathbf{L}$ and its symmetric part $\mathbf{D}$ tensors are defined in the global coordinate system C_0 with three orthogonal principal axes $\mathbf{x}_i$ aligned with ED, TD and ND, respectively, as shown in Fig. 2.

Following earlier works [2, 6, 15], a co-translating and co-rotating coordinate system C' is defined at each point along the material paths. An orthonormal coordinate frame C' is defined locally with $\mathbf{x}'_1$ in the flow direction (tangent to the path line, parallel with

$\mathbf{v}$). Due to the axis-symmetry, the flow path of the steady flow defines a flow surface. The second axis $\mathbf{x}_2'$ is defined normal to this axis-symmetric flow surface, and $\mathbf{x}_3'$ is defined in the flow surface and normal to $\mathbf{x}_1'$ and $\mathbf{x}_2'$. The two coordinate systems C_0 and C' are related by a rotation tensor $\mathfrak{R}$ as $\mathbf{x}_i = \mathfrak{R}^{\mathrm{T}} \cdot \mathbf{x}_i'$, where the superscript 'T' denotes a transposed matrix. It is noted that the coordinate frame C' changes with time, i.e. $C'(t)$, and at the end of extrusion the local C' and the global C_0 coordinate systems are identical. The rate of deformation tensor in the local coordinate system is then expressed as $\mathbf{D}' = \mathfrak{R}^{\mathrm{T}} \cdot \mathbf{D} \cdot \mathfrak{R}$. The diagonal components of $\mathbf{D}'$ represent the instantaneous stretching rates of three material elements e_i' which are parallel with $\mathbf{x}_i'$ at the time *t*, while the off-diagonal components represent the shear rates which are corresponding to angle changes among material elements, see Fig. 2. At any time *t*, the path length that a material point needs to travel to reach the end of the path line, is calculated as

$$\Gamma = \int_{t_s}^{t_e} v(t)dt - \int_{t_s}^{t} v(t)dt \tag{3}$$

where $v(t)$ is the particle velocity and t_s and t_e are the starting and ending time of extrusion, respectively, with $t_s < t < t_e$.

The co-rotational integration of $\mathbf{D}$ [16] provides the deformation tensor $\boldsymbol{\varepsilon}^{\mathrm{R}}$, which is calculated for each particle path as a measure of the accumulated deformation. More details of the tensor $\boldsymbol{\varepsilon}^{\mathrm{R}}$ and its calculation can be found in the book [16] and are summarized in Appendix A.

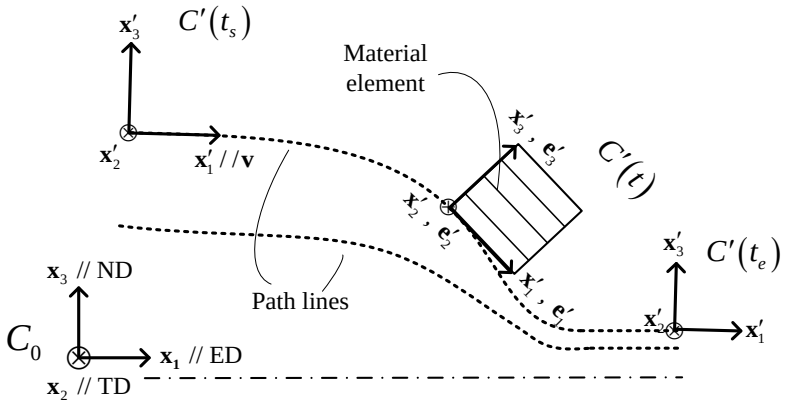

Fig. 2 Deforming an infinitesimal material element in a steady axisymmetric flow. The materials vectors e_i' are defined in a co-translating and co-rotating coordinate system C', while the global frame C_0 is fixed.

4. Results

4.1. Experimental results

The extrusion microstructure of the round profile is shown in Fig. 3. The colours are coded according to the ED direction inverse pole figure (IPF), hence grains of the <111> fibre and the <100> fibre texture components are coloured blue and red, respectively. The <*uvw*> fibre texture component here is defined by that an <*uvw*> direction in the local crystal coordinate system of a considered grain has an orientation deviating less than 15° from the ED direction. As shown in Fig. 3 (a), the overall through thickness microstructure exhibits fibrous grain morphology. By a smaller step size in EBSD, a microstructure with very elongated high-angle grain boundaries (HAGB, >15°) and nearly equiaxed subgrains with low-angle grain boundaries (LAGB, 2-15°) [17] is shown in both Fig. 3 (b) and (c), for small representative areas in Sec. I and III, respectively. Only a few grains, which are found to be subgrain-free, are here larger than 10 µm and close to equiaxed shape. These are pointed out by arrows in Fig. 3 (c). However, the number of such grains and their area fraction are small. Hence, the microstructure of the main part of the extruded round profile is in the as deformed state.

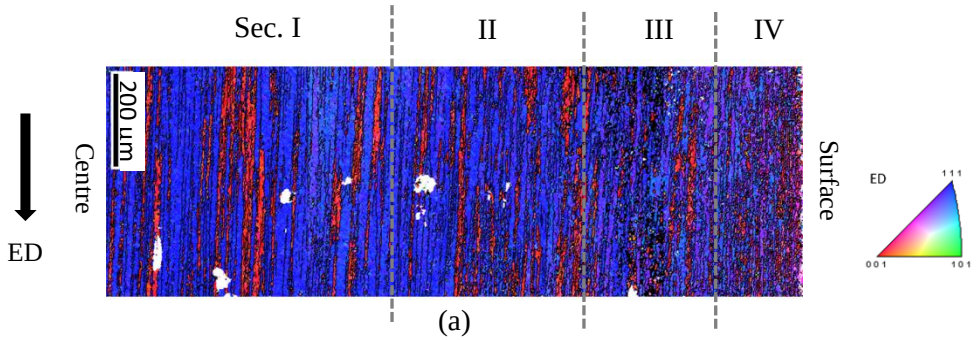

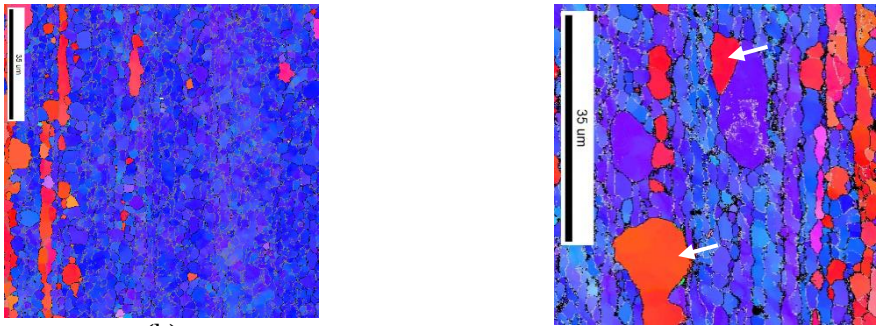

(b) (c)

Fig. 3 EBSD micrographs of the microstructure of profiles extruded, (a) overall microstructure from the central to the surface, (b) a fine scan showing substructure of a small area in Section I and (c) a fine scan from Sec. III. The black lines represent HAGB (>15°), while LAGB (2-15°) is represented by grey lines in (b) and (c).

The measured {100} and {111} pole figures are shown in Fig. 4 for the overall area, and in Fig. 5 for sections across the thickness. As can be seen from Fig. 12, the overall duplex fibre texture consists of a <111> fibre that is about 4 times stronger than the <100> fibre. The textures of the two centre regions, i.e. Sec. I and Sec. II, are very similar. Further towards the surface, the <100> fibre gradually weakens. The intensity of the <100> fibre decreases to about the random level in the surface region, Sec. IV. Compared to these two regions closest to the centre, the <111> fibre is weakened and rotated from its ideal position when approaching the surface regions. Especially for Sec. IV, grains with the <223> crystallographic axis parallel with ED, i.e. the <223> fibre, contribute to the main texture component.

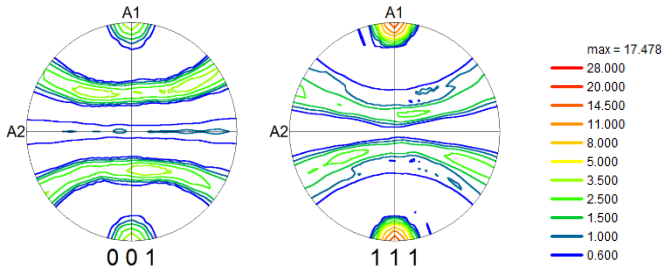

Fig. 4 Overall texture of extruded round profile (A1 - ED, A2 - TD)

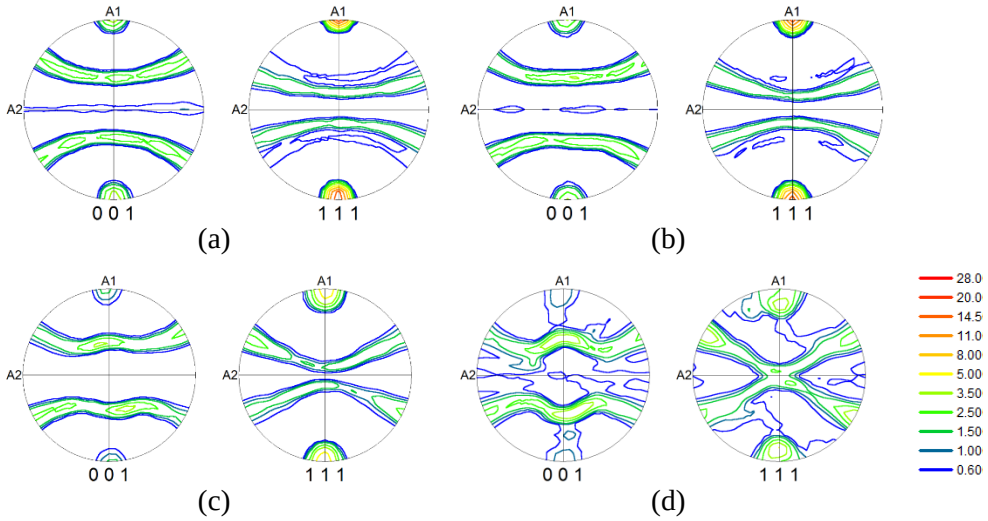

Fig. 5 Measured texture for Sec. I (a), Sec. II (b), Sec. III (c) and Sec. IV (d). (A1 - ED, A2 - TD)

4.2. Deformation mode analysis

The deformation with its through-thickness variation can be analyzed based on the FEM flow simulation. Evolutions of accumulated strains ε along selected particle paths are illustrated in Fig. 6 for the four particle paths with s = 0.05, 0.55, 0.80 and 0.95. The two vertical dash lines mark the starting and ending positions of the recessed pocket for one of the paths, with s=0.05. As shown in Fig. 6, the final accumulated strain increases from the center to the surface, while it is about 1.5 times higher in the profile for path s = 0.95 than for path s = 0.05. The strain accumulates slowly behind in the billet. At $\Gamma = 10$ mm, the strain still remains less than one fourth of the final strain. Close to the pocket, i.e. when $\Gamma < 10$ mm, the strain increases rapidly.

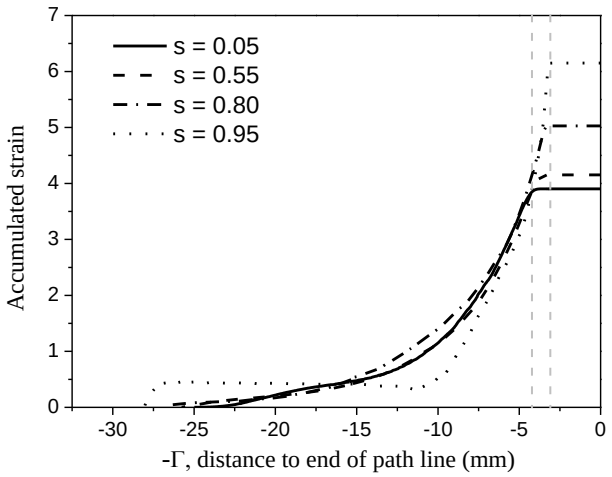

Fig. 6 Evolution of accumulated strains for four different particle path lines by FEM simulations.

The D'_{11}, D'_{33} and D'_{13} rate of deformation tensor components in the local coordinate system are shown for four particle paths in Figs. 7-10. The figures include close-ups for the region $\Gamma > 10$ mm, in which the deformation rates are considerable smaller than the peak values at the outlet. Similar as in Fig. 6, the two dashed lines indicate the starting and ending position of the pocket in Figs. 7-10. The other two shear deformation related components D'_{12} and D'_{23} are negligibly small, while the component D'_{22} follows from volume conservation during plastic deformation.

The deformation during extrusion is non-monotonic. For example, the D'_{11} component, which represents the instantaneous stretching rate along the local flow direction, has a value less than 1 /s at the rear of the billet, whereas its peak value is about 100 /s for the two central paths, about 200 /s for the path s=0.80, and about 600 /s for the surface path s=0.95. The centre path reaches its peak of deformation rate before reaching the pocket, whereas for the other three paths, the corresponding position of the D'_{11} peak moves into the pocket. In particular for the path s = 0.95, the peak value of D'_{11} is located at the exit of the pocket.

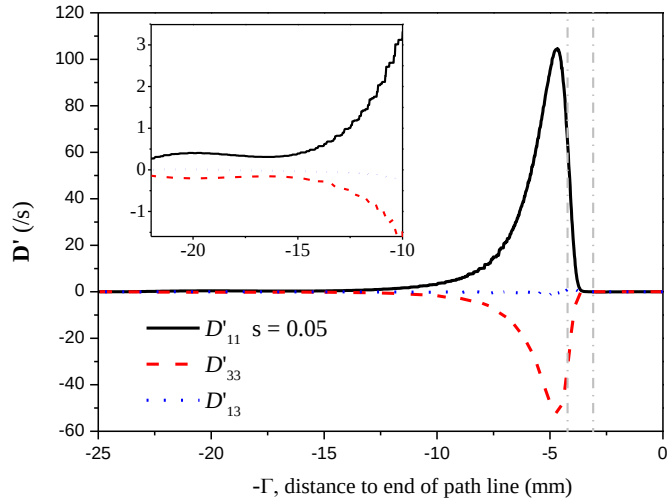

(a)

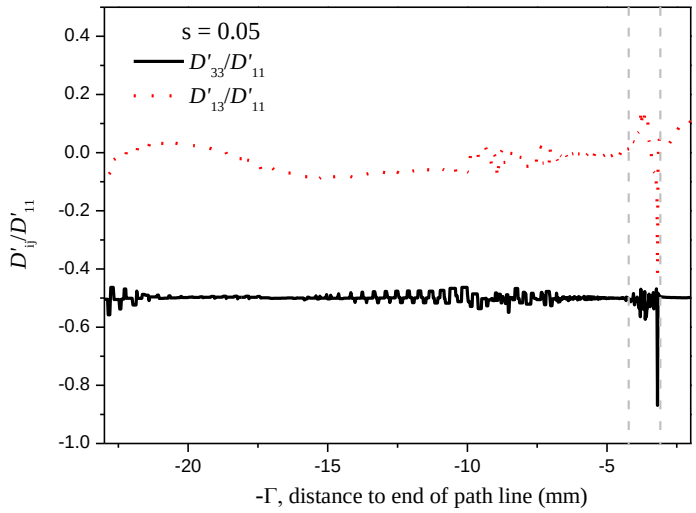

(b)

Fig. 7 Deformation mode analysis for the particle path s 0.05, (a) plot of components of the deformation rate tensor $\mathbf{D}'$ and (b) ratios between these components, in the local frame attached to the path line

The in-plane shear deformation-rate component D'_{13} remains almost zero along the path s = 0.05, indicating no shear deformation at the centre of the profile. The ratios D'_{33} / D'_{11} and D'_{13} / D'_{11} are plotted in Fig. 7 (b). The ratio D'_{13} / D'_{11} remains very close to zero, as shown in Fig. 7 (a). The ratio D'_{33} / D'_{11} remains -0.5, with some numerical

noise. The deformation type for the centre path is thus as for uniaxial tensile deformation with r-value equal to unity.

For the path s=0.55 in Fig. 8, the component D'_{13} have some values different from zero in the region before entering the pocket, but the average value of $|D'_{33} / D'_{11}|$ remains smaller than 0.1 for the region $\Gamma < 10$ mm, where the strain accumulates rapidly. The negative value of D'_{13} means, that the flow velocity is smaller than towards the surface. The ratio D'_{33} / D'_{11} for the path s=0.55 is very similar as that for s=0.05.

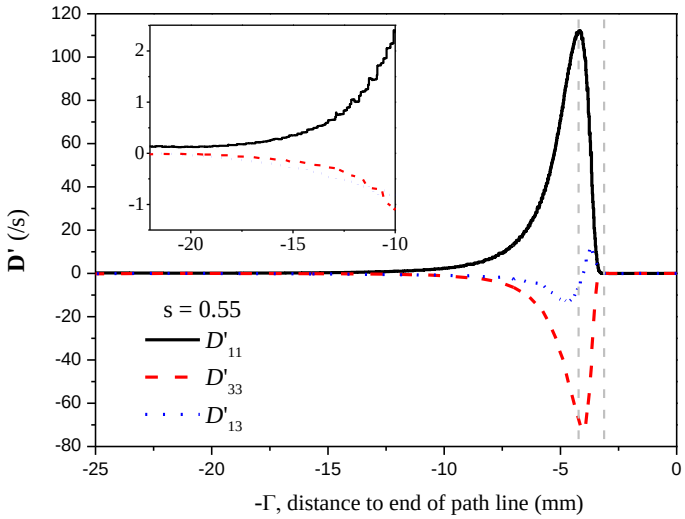

Fig. 8 Deformation mode analysis for the particle path s = 0.55, plot of components of the deformation rate tensor $\mathbf{D}'$ in the local frame attached to the path line

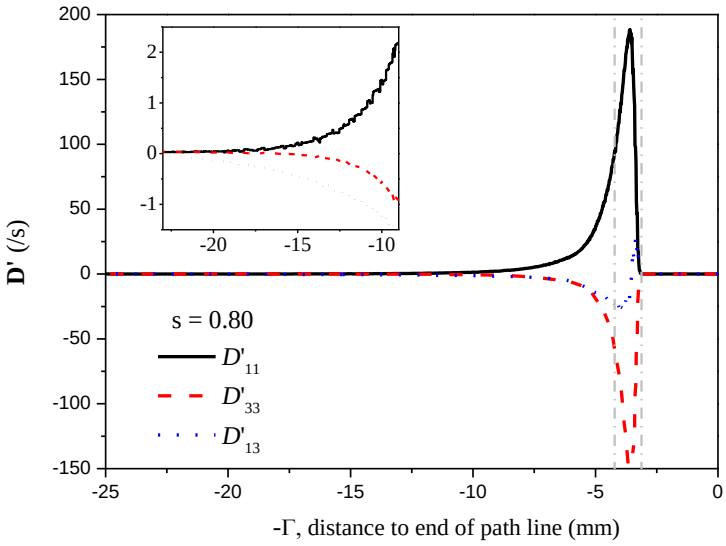

(a)

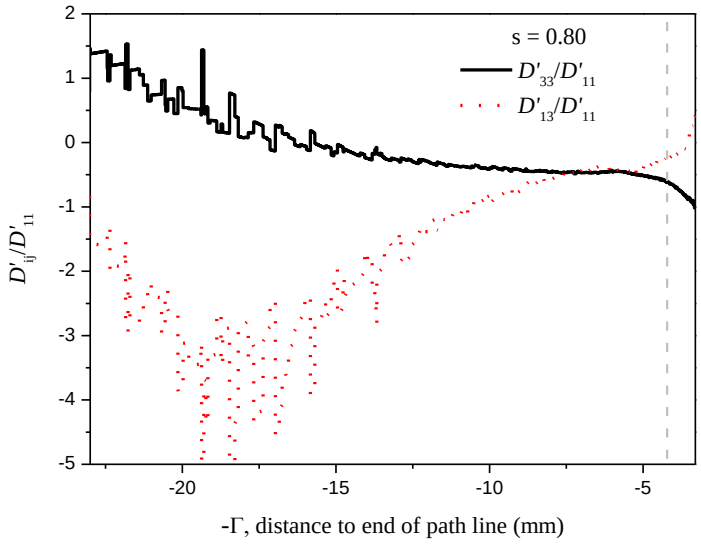

(b)

Fig. 9 Deformation mode analysis for the particle path s = 0.80, (a) plot of components of the deformation rate tensor $\mathbf{D}'$ and (b) ratios between these components, in the local frame attached to the path line

For the path s=0.8 in Fig. 9, the shear component D'_{13} becomes relatively strong upstream towards the inlet of the pocket, However, D'_{13} increases more slowly than the diagonal component D'_{13}/D'_{11}. It is also interesting to see that the ratio $\left|D'_{33}/D'_{11}\right|$

changes sign when following the particle path from the rear of the billet into the pocket and bearing. At the rear of billet, both D'_{11} and D'_{33} are positive valued, indicating a compression mode along the TD, whereas for $\Gamma < 15$ mm, the material is stretched along the flow direction and contracts in the corresponding transverse directions in the local frame. Inside the pocket, the deformation mode is close to plane strain tension, with some small shear contributions.

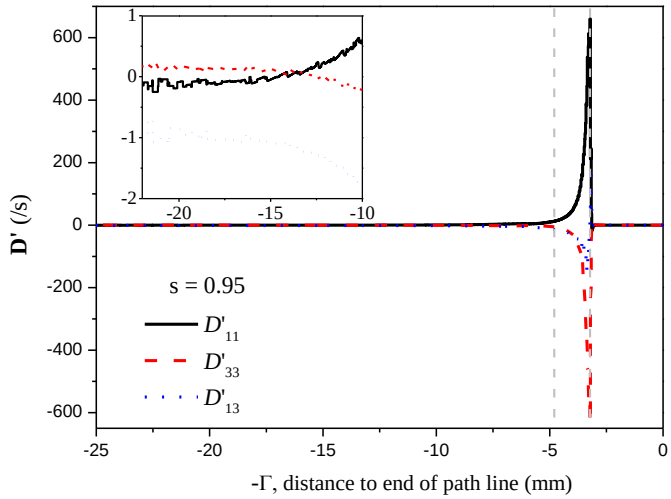

Fig. 10 Deformation mode analysis for the particle path s = 0.95, plot of components of the deformation rate tensor $\mathbf{D}'$ in the local frame attached to the path line

For the path s=0.95, the deformation components are plotted in Fig. 10. The magnitude of the shear component is higher than the diagonal components until very close to the pocket. Since D'_{33} / D'_{11} is close to -1.0 in the pocket, the dominating mode is plane strain tension, but with superimposed shear deformation.

The calculated deformation tensor $\boldsymbol{\varepsilon}^{R}$ components are compiled in Table 3, which gives information about the final state of deformation. As concluded by the above analysis for the path s = 0.05, it is close to ideal uniaxial tensile deformation. When approaching the surface, the component ε^{R}_{13} increases. Especially at the very surface region, corresponding to the Sec. IV, the shear component is comparable to the stretching strain along the flow direction.

It is also interesting to observe that $\varepsilon_{22}^{\mathrm{R}}$ is constant through the thickness. The relative position of the material point in the billet at the beginning of extrusion is also calculated, defined as s_{billet}, i.e. the distance to the centre divided by the radius of the billet. The relative position in the billet is the same as is the profile, which explains the constant $\varepsilon_{22}^{\mathrm{R}}$ through the thickness[‡].

The component $\varepsilon_{11}^{\mathrm{R}}$ increases from the centre towards the surface. In the surface region $\varepsilon_{22}^{\mathrm{R}}$ is nearly equal for all paths, and the ratio $\varepsilon_{33}^{\mathrm{R}} / \varepsilon_{11}^{\mathrm{R}}$ decreases from -0.5 towards -1 extrapolated to the surface. This is consistent with the above analysis for the paths s =0.80 and 0.95, i.e. close to plane strain tension with superimposed shear deformation in the pocket.

Table 3 The deformation tensor $\boldsymbol{\varepsilon}^{\mathrm{R}}$

Paths	$\varepsilon_{11}^{\mathrm{R}}$	$\varepsilon_{22}^{\mathrm{R}}$	$\varepsilon_{33}^{\mathrm{R}}$	$\varepsilon_{13}^{\mathrm{R}}$	$\left\|\varepsilon_{12}^{\mathrm{R}}\right\|$, $\left\|\varepsilon_{23}^{\mathrm{R}}\right\|$	s_{billet}
s=0.05	4.06	-2.03	-2.03	-0.02		0.05
s=0.55	4.22	-2.01	-2.21	-0.26		0.55
s=0.80	4.85	-2.02	-2.83	-0.81	< 0.01	0.80
s=0.90	6.16	-2.03	-4.13	-2.45		0.90
s=0.95	8.26	-2.08	-6.18	-5.76		0.95

Ideally, $\varepsilon_{11}^{\mathrm{R}}$ should be the same as the accumulated strain ε for the path s =0.05, i.e. 3.9. The about 3% difference between them is probably caused by the accumulation of numerical errors when integrating the $\boldsymbol{\varepsilon}^{\mathrm{R}}$ over about 1000 time steps.

[‡] Imagine a batch of concentric arcs have the same infinitesimal subtended angle θ at the centre, which are perpendicular with the ED and share the same centre as the billet/profile. After extrusion, that subtended angle θ has to be preserved to keep the symmetry of circle. The contraction of the length of act hence equals then to the contraction of the radius. Therefore, the same relative positions in the billet and profiles for all paths will result in the same transverse deformation.

4.3. Deformation texture modelling by coupling crystal plasticity and FEM

The simulated temperature close to the surface in the middle of the bearing channel was 373.4 °C, while the temperature recorded by the thermocouple in the bearing channel was about 400 °C near the end of the extrusion process. The temperature from the FEM flow simulation compared well to the experimental results.

The predicted deformation textures by the FC-Taylor and the Alamel models are shown in Fig. 11, for the overall area and for the four different through-thickness sections. Similar as the experimental ones, a duplex <111> and <100> fibre texture is predicted by both models for all sections except the surface region. For Sec. IV, the FC-Taylor model predicted a strong {101}<445> texture. The Alamel model predicted a similar texture component as the FC-Taylor for Sec. IV, but much weaker.

Fig. 12 gives the maximum intensity of the <111> and <100> fibres, by which the predicted textures can be compared to each other and to the experiments. Both CP models predicted a strong <111> and weak <100> fibre through the thickness, similar as the experiments, but the predictions are sharper than the experiments in terms of intensities of fibres. The Alamel prediction is closest to the experiments. Similar as for the experiments, the intensities of the <111> and <100> fibres decrease at sections III and IV, compared to the centre. The predicted <100> fibre by the two CP models are less than random for Sec. IV.

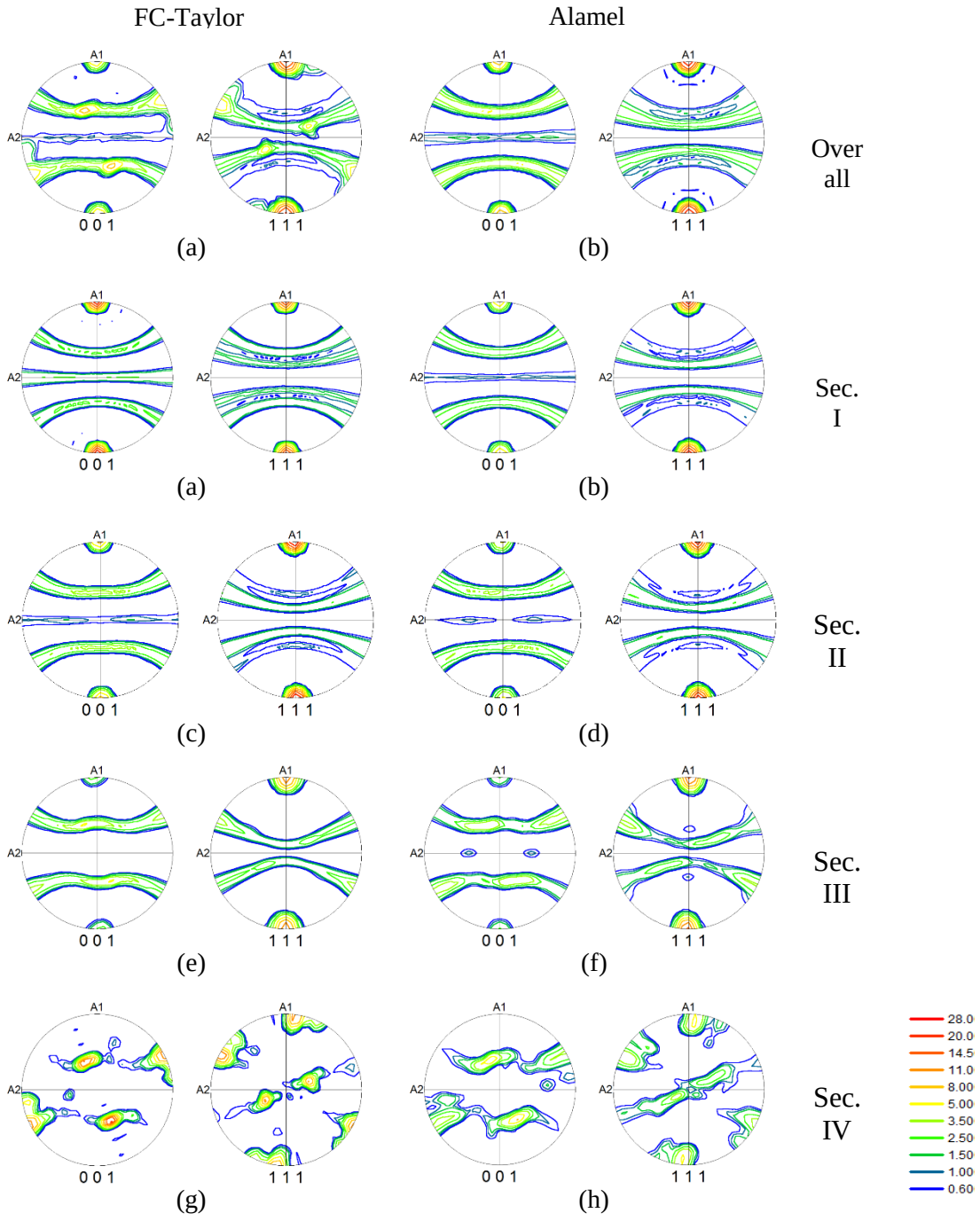

Fig. 11 Deformation texture predicted by FC-Taylor and Alamel models for the overall area and four different sections. (A1 - ED, A2 - TD)

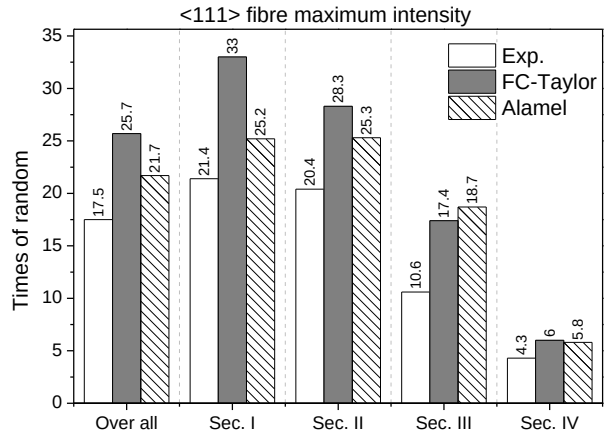

(a)

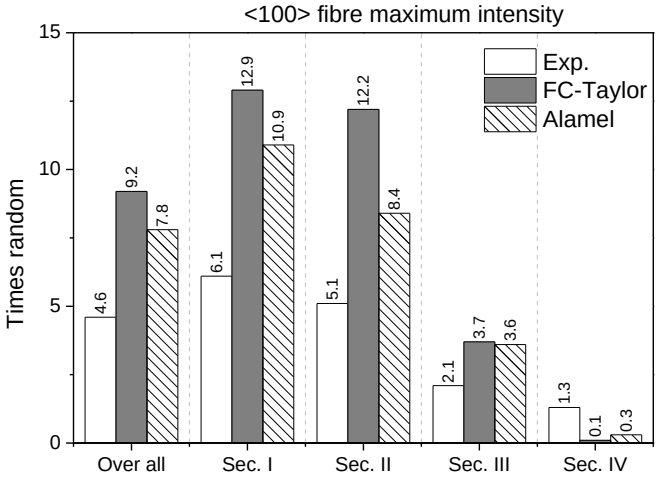

(b)

Fig. 12 Maximum fiber intensity by experiments and crystal plasticity modelling, (a) the <111> fibre and (b) the <100> fibre

The normalized texture difference ID_N is calculated for comparison of all CP predictions to their experimental counterparts. The results are compiled in Table 4. The smaller the ID_N, the better the prediction is.

The performance of the two CP models with respect to the deformation texture predictions can then be compared in a quantitative manner by the values of the normalized difference texture index, ID_N, as presented in Table 4. The Alamel clearly outperforms the FC-Taylor model for all through-thickness sections.

Predictions with ID_N less than 20% are considered being in very good agreement with the experiments here. Note that a portion in Euler space with $\varphi_1 = 0 - 360°$ is considered. Predictions with ID_N larger than 100% could indicate that the main texture components are missed in the predictions, while predictions with ID_N between 20%-100% are considered as modest in this work. Hence, the FC-Taylor texture predictions are very good for the overall area, modest for the central three sections and of low quality for the surface region. The Alamel model gives very good predictions of deformation texture for the overall, Sec. I and Sec. II, and the predictions are modest for the two outer sections, when compared to the experiments.

Table 4 Evaluation of deformation texture predictions by ID_N

	ID_N	
	FC-Taylor	Alamel
Over all	13.3%	6.2%
Sec. I	36.1%	17.4%
Sec. II	29.4%	13.3%
Sec. III	57.9%	47.4%
Sec. IV	600%	100%

5. Discussion

The water-quenched profile is essentially in the deformed state, whereas few grains are found recrystallized. The area fraction of such grains is higher at the surface region than the centre, as shown in Fig. 3, which could be attributed to the higher peak strain-rates and larger accumulated strains near the surface than at the centre, as illustrated in chapter 4.2. The FEM flow simulation predicted an almost uniform temperature field along the thickness in the pocket, with only a few degrees higher at the surface than in the inner regions, hence limited effects are expected on the recrystallization behaviours observed.

Two sharp fibre texture, i.e. the <111> and the <100> fibre, developed in the centre regions of the round profile, i.e. Secs. I and II. The <111> fibre is about four time stronger than the <100> counterpart, as shown in Fig. 12. Such a strong <111> and

<100> duplex fibre texture has been reported earlier in the literature, for the extrusion of aluminium rods [1, 5], copper wire drawing [18] and tension deformation of FCC metals [19] etc.. The deformation analysis based on the FEM flow simulation demonstrates clearly that it very close to uniaxial tension mode for the path s=0.05. The deformation at path s=0.55 is very similar to that for the path s=0.05. For these two paths, the shear deformations (i.e. D'_{13} and ε^{R}_{13}) are all negligibly small, while the contraction along the radial directions is half of the elongation along ED, as evident from Fig. 7 - Fig. 8 and Table 3. Theoretical treatments of the texture development predict orientations which have three or more equally stressed slip systems symmetrically arranged with respect to the major flow direction. Thus a major <111> texture and a secondary, less-stable <001> texture have been predicted for all FCC metals [5, 20]. However, the texture, for example its relative strength of the <111> and <100> fibre, is found to be alloy (stacking fault energy) [19], deformation temperature [1] and strain dependent [18].

Through thickness variations of the deformation texture in extruded aluminium rods have earlier been reported in the literature. Vatne et al. [1] observed that the <111> and <100> fibre texture components were strongly rotated when approaching the surface, and attributed such rotations of fibre textures to the strong shear deformation at the surface. At the surface of an extruded aluminium rod, Lee et al. [5] claimed that the fibre texture no longer existed, but was replaced by {110} <335>, where {110} corresponds to the plane normal to the radial direction of the rod and <335> to the direction parallel to the rod axis. Similar texture components were also observed by Vatne et al. [1]. The experimental results of the near surface regions, i.e. Fig. 5 (c) and (d) for the Sec. III and IV, respectively, show similarities to that reported in the literature, i.e. that the fibre texture is rotated or distorted. Especially for the Sec. IV, it is found that most grains have their <223> axis along the ED, which is almost identical as <335>. However, it is still a fibre texture, <223> fibre, instead of preferring the <110> axis along the radius direction. In the current work, the surface texture is observed in Sec. IV, which covers from s=0.90 to the very surface, whereas Lee et al. [5] directly measured on the very surface. In our work, the deformation texture in the surface region, i.e. Sec. IV, is considered, rather than the surface texture.

The reported {110}<335> surface texture is not so far from the {011}<211> Bs deformation texture, which develops during rolling of FCC metals. Lee et al. [5] analysed the deformation during rod extrusion. Maintenance of circles in transverse sections before and after reduction indicates that the transverse strain is homogeneous, which agrees well with our deformation analysis based FEM flow simulation, i.e. the same values of $\varepsilon_{22}^{\mathrm{R}}$ along the thickness in Table 3. The homogeneity of $\varepsilon_{22}^{\mathrm{R}}$ is alternatively explained in Section 4.2 by the same relative position in the billet and in the profile there.

By schematic grid patterns in the billet before and after extrusion, Lee et al. [5] illustrated that the deformation can be close to plain strain tension at the surface, when the radial strain is very large compared with the transverse strain. The finding by Lee et al. [5] is partially supported by the deformation analysis presented in Section 4.2. As shown in Fig. 9 and Fig. 10, the ratio D'_{33} / D'_{11} is close to -1.0 in the pocket, and also the ratio $\varepsilon_{33}^{\mathrm{R}} / \varepsilon_{11}^{\mathrm{R}}$ gets closer to -1.0 when moving towards the surface. Hence, it is close to plane strain tension if the shear strains were negligible. However, it is not the case here. The shear deformation $\varepsilon_{13}^{\mathrm{R}}$ is comparable to $\varepsilon_{11}^{\mathrm{R}}$ for paths s=0.90 and 0.95 in Table 3. Therefore, it is close to the plane strain tension with superimposed shear deformation (simple shear) for the surface layers.

By coupling the FEM flow simulation with crystal plasticity models, the deformation texture and its through thickness variation were separately predicted by the FC-Taylor and the Alamel model. Both models gave good predictions for the inner three sections, where a duplex fibre texture with strong <111> and weak <100> is obtained. For the Sec. IV, the FC-Taylor and the Alamel model predicted a strong and a rather weak {101}<445> texture, respectively. The predictions are similar to the experimental data for the surface texture reported in the literature [5], but different from the current experimental data which shows a <223> fibre texture. Quantitative comparisons between the predictions and the experimental texture are shown in Fig. 12 and Table 4. The Alamel model clearly outperforms the FC-Taylor model. The Alamel model allows certain relaxations on the strain constraint with addition requirements for stress equilibrium, which is more physically realistic than the iso-strain FC-Taylor model, hence it shows a better performance for predicting deformation texture [13] or plastic anisotropy [21].

The Alamel model with the so-called Type III relaxation (Alamel-T3) [14] and the visco-plastic self-consistent model with the Tangent linearization scheme (the instantaneously strain-rate sensitivity 0.1) [22] were also employed for the deformation texture predictions. The Alamel-T3 model predictions are similar to the Alamel for the three inner three section, but a strong <111> fibre texture is wrongly predicted for Sec. IV, with a maximum intensity for the <111> fibre as 16 times random. The VPSC predictions of the <111> fibre is similar to that of Alamel-T3, with the maximum intensity for the <111> fibre as 8 times random for Sec. IV. However, the VPSC predicted a much stronger <100> fibre texture for all section. The relative ratio between the intensities of the <111> and the <100> fibre is close to one for all sections. The stronger <111> fibre by the Alamel-T3 and the VPSC for Sec. IV may be due to stronger relaxations of strain-constraints, especially on the in-plane shear, than the Alamel and the FC-Taylor model. The much stronger <100> fibre texture predicted by the VPSC than the other three model may be due to that not only the constraints on the shear components are relaxed, but also the diagonal components. Crystal plasticity FEM (CPFEM) can better account for the strain heterogeneities across the grain aggregates [23], but coupling CPFEM with extrusion deformation histories is not straightforward. The Alamel model performed the best among the crystal plasticity model considered here for the texture prediction.

The deformation history from the FEM flow simulation is one of the key input for crystal plasticity models when predicting deformation texture. The quality of the FEM flow simulation will then influence the texture predictions. A more realistic flow simulation, for example using finer FEM mesh and considering the transient dynamic deformations, may improve the accuracy of the deformation fields and thus improve the quality of the texture predictions.

6. Conclusion

This paper presents comprehensive studies on the deformation texture and deformations, and their through-thickness gradients, for extruded aluminium round profiles. Measured by the EBSD, the deformation texture is a strong <111> and weak <100> duplex fibre texture in the centre of the profile, but rotated when approaching the surface. The deformation histories were taken from the FEM flow simulations. Analysing the deformation qualitatively by the $\mathbf{D}'$ in the local frame and by the

deformation tensor $\boldsymbol{\varepsilon}^R$ (the corotational integration of $\mathbf{D}$), it is close to an ideal uniaxial tensile deformation mode for the materials traveling in the centre of the billet and profile, while it is found close to plane-strain tension deformation mode with superimposed simple shear deformation for the surface region. The deformation texture can be well predicted by coupling the FEM flow simulation and the crystal plastic model for Secs. I-III. For the surface layer, the texture predictions by the FC-Taylor and the Alamel model are only qualitatively correct. The Alamel model is the best model for the texture predictions for the current study.

Acknowledgement

This research work was supported by the IPN project COSMETEX (228918/O30) in Norway. The financial support by the Research Council of Norway and the industrial partner SAPA AS (now Hydro Extruded Solutions) is gratefully acknowledged.

Appendix A Corotational integration of deformation rate

This chapter summarizes the corotational integration of deformation rate which is detailed in the reference [16]. Due to large rotations during finite deformation, it is generally meaningless to carry out the integration $\int \mathbf{D}dt$. This integration equals the logarithmic strain only when the principle axes of the stretches are fixed in spaces. Such a coordinate frame C^{m} having the principle material stretch axes as the coordinate axes can be defined by a rotation tensor $\mathbf{R}$ out of the polar decomposition of the deformation gradient tensor $\mathbf{F}$. It is noted that the rotation tensor $\mathbf{R}$ is not the same as the rigid body rotation tensor $\mathfrak{R}$ in Section 3.3, which relates the frames C' and C_0. The $\mathbf{F}$ tensor is incrementally calculated by the velocity gradient tensor $\mathbf{L}$ through the relationship that $\dot{\mathbf{F}} = \mathbf{L} \cdot \mathbf{F}$.

The integration of **D** is carried out directly in the frame C^{m}, but is transformed to the global frame at the end of deformation to give the corotational integration of **D**, which is termed as $\boldsymbol{\varepsilon}^{\mathrm{R}}$

$$\boldsymbol{\varepsilon}^{\mathrm{R}}(t_e) = \mathbf{R}(t_e) \cdot \left[\int_{t_s}^{t_e} \mathbf{R}^{\mathrm{T}}(t) \cdot \mathbf{D}(t) \cdot \mathbf{R}(t) dt \right] \cdot \mathbf{R}^{\mathrm{T}}(t_e) \tag{4}$$

where t_s and t_e are the starting and ending time of deformation, respectively, and $t_s < t < t_e$.

Reference

[1] H.E. Vatne, K. Pedersen, O. Lohne, G. Jenssen, Textures Microstruct., 30 (1997) 81-95.
[2] T. Aukrust, S. Tjøtta, H.E. Vatne, P. Van Houtte, Int. J. Plast., 13 (1997) 111-125.
[3] T. Furu, H.E. Vatne, Mater. Sci. Forum, 273-275 (1998) 8.
[4] S. Abis, R. Caciuffo, R. Coppola, Mater. Lett., 6 (1988) 423-426.
[5] L. Dong Nyung, C. Yong Hoon, S. Myung Chul, Scripta Metallurgica, 17 (1983) 339-342.
[6] F. Pérocheau, J.H. Driver, Int. J. Plast., 16 (2000) 73-89.
[7] K. Zhang, K. Marthinsen, B. Holmedal, T. Aukrust, A. Segatori, Materials Today: Proceedings, 2 (2015) 4898-4903.
[8] C.M. Sellars, W.J.M. Tegart, International Metallurgical Reviews, 17 (1972) 1-24.
[9] T. Sheppard, D.S. Wright, Metals Technology, 6 (1979) 215-223.
[10] M.P. Clode, Fifth International Aluminium Extrusion Technology Seminar, Wauconda, IL, 1992, pp. 79-99.
[11] T. Sheppard, A. Jackson, Mater. Sci. Technol., 13 (1997) 203-209.
[12] P. Van Houtte, Textures Microstruct., 8 (1988) 313-350.
[13] P. Van Houtte, S. Li, M. Seefeldt, L. Delannay, Int. J. Plast., 21 (2005) 589-624.
[14] T. Mánik, B. Holmedal, Mater. Sci. Eng., A, 580 (2013) 349-354.
[15] H.H. Winter, Journal of Non-Newtonian Fluid Mechanics, 10 (1982) 157-167.
[16] A.S. Khan, S. Huang, Continuum Theory of Plasticity, John Wiley & Sons, New York, 1995.
[17] Y.C. Lin, X.-Y. Wu, X.-M. Chen, J. Chen, D.-X. Wen, J.-L. Zhang, L.-T. Li, J. Alloys Compd., 640 (2015) 101-113.
[18] I. Inakazu, Y. Kaneno, H. Inoue, Mater. Sci. Forum, 157-162 (1994) 715-720.
[19] E.A. Calnan, Acta Metall., 2 (1954) 865-874.
[20] G.I. Taylor, J. Inst. Metals., 62 (1938) 307-324.
[21] K. Zhang, B. Holmedal, O.S. Hopperstad, S. Dumoulin, J. Gawad, A. Van Bael, P. Van Houtte, Int. J. Plast., 66 (2015) 3-30.
[22] R.A. Lebensohn, C.N. Tomé, Acta Metall. Mater., 41 (1993) 2611-2624.
[23] L.-T. Li, Y.C. Lin, L. Li, L.-M. Shen, D.-X. Wen, J. Mater. Eng. Perform., 24 (2015) 1294-1304.